COMMUNICATIONS CHEMISTRY

ARTICLE

https://doi.org/10.1038/s42004-019-0238-9 OPEN

Bioinspired networks consisting of spongy carbon wrapped by graphene sheath for flexible transparent supercapacitors

Duc Dung Nguyen [1], Chung-Hsuan Hsiao[1], Teng-Yu Su[1], Ping-Yen Hsieh[1], Yu-Ling Chen[1], Yu-Lun Chueh [1], Chi-Young Lee[1] & Nyan-Hwa Tai[1]*

Hierarchically ordered structures with low tortuosity, excellent mechanical flexibility, high optical transparency, and outstanding electrical conductivity are critically important in developing flexible transparent supercapacitor electrodes for innovative applications in electronics and displays. Here a CVD process is employed to fabricate leaf-skeleton inspired electrodes, which are reticulated monolithic networks consisting of carbon nanostructures serving as a 3D spongy core and graphene-based films as a protective/conductive shell. The network electrodes show optical transmittance of 85–88%, an electrical sheet resistance of ~1.8 Ω/sq, and an areal capacitance of 7.06 mF cm^{-2} (at 0.78 mA cm^{-2} in a three-electrode cell) in Na_2SO_4 aqueous electrolyte. Flexible transparent and symmetric supercapacitors, based on PVA/H_3PO_4 gel and the network electrodes, possess a stable working voltage of 1.6 V, energy and power density of 0.068 μWh cm^{-2} and 47.08 μW cm^{-2} at an optical transparency of ~80%, and no capacitance loss over 30,000 flat-bend-release cycles.

[1] Department of Materials Science & Engineering, National Tsing-Hua University, Hsinchu 30013, Taiwan. *email: nhtai@mx.nthu.edu.tw

With the rapidly growing markets of modern electronic technologies, greater demands on portable, flexible, and fully transparent devices are pushing traditional built-in power supplies towards flexibility and transparency[1–4]. Over past decades, supercapacitors (SCs) have emerged as prominent power supplies because of their high power density, fast charge/discharge rate, and long cycle life[4,5]. Adding flexibility and transparency to SCs is commonly accomplished via designing their electrodes with flexible transparent, conductive, and capacitive/pseudocapacitive properties. A common approach to construct flexible transparent SC electrodes is the deposition of active materials onto flexible transparent conductive electrodes (TCEs) with rigorous attention paid to adjustment of mass loading in order to achieve highest areal capacitance at lowest deterioration in optical transmittance[1,3]. In this context, transition-metal oxides, such as manganese oxide (MnO_2), have been considered the most selected active materials owing to their high theoretical capacitance, environmental benignity, and nature abundance[3,6–8]. However, poor electrical conductivity and rapid capacitance degradation of MnO_2 due to large volume expansion/contraction during repeated charge/discharge processes hamper its practical uses in energy storage[9–12]. It is worth noting that such volume alterations after few thousand charge/discharge cycles could lead to dissolution and fragmentation of MnO_2 into colored, segregated nanoparticles[9,10]; therefore, optical transparency of MnO_2-based SCs should be seriously deliberated if severe conditions, such as long time operation under flexed states are employed. Another efficient strategy to obtain flexible transparent SC electrodes with large areal capacitance is the direct utilization of conductive and capacitive/pseudocapacitive materials, such as $Ti_3C_2T_x$ nanosheets[2], RuO_2/PEDOT:PSS[13], and PEDOT:PSS[14] in the form of thin films. Nevertheless, the intrinsic operation voltage of these active materials are moderately narrow (0.6–0.8 V), thus hindering achievement of high-energy density devices[5].

Owing to their fascinating properties such as large surface area, excellent chemical stability, high conductivity, good flexibility, and ultralight weight, carbon nanomaterials have been extensively explored as both efficient active materials and flexible TCEs for SCs[15–26]. Although highly transparent carbon-based SCs have been demonstrated to perform excellent cycle stability and ultrahigh rate, their areal capacitances and energy densities are low[20–23]. A possible elucidation lies in designed configurations of the carbon-based SC electrodes, where carbon nanomaterials are generally assembled as ultrathin and compactly planar films (for high transparence and structural robustness), thus only top surface of outermost layers is available for electrolyte ions accessing (i.e., limited ion-accessible surface area). In this regard, highly ordered carbon-based assemblies such as films of three dimensionally (3D) interconnected carbon nanomaterials are desirable structures because of their large ion-accessible surface areas[17,24]; yet, development of such spongy film electrodes with flexible transparent features has not been demonstrated.

Here we present a bioinspired strategy to fabricate freestanding and flexible transparent networks as SC electrodes in a one-step growth process using a conventional chemical vapor deposition (CVD) method. The electrodes are hierarchical reticulated monolith of leaf-skeleton mimicked conduits, which consist of interconnected carbon nanostructures (hereafter referred to as nanocarbons) serving as a 3D spongy carbon core and graphene-based films (graphene–Ni or graphene) as a protective and conductive shell. In other words, the 3D spongy carbon core, acting as the main active material, is well-preserved inside the robust graphene shell, which functions as both active material and flexible TCE. Thereby, fragmentation of the main active material during charge/discharge cycles and/or by unexpected mechanical shocks can be certainly minimized. Moreover, the leaf-skeleton mimicked and core–shell (LSMCS) electrodes, regarded as a bioinspired microfluidic network, could provide interconnected channels for electrolyte ions transporting throughout and contacting entirely with the 3D spongy carbon core and interior/exterior surfaces of the graphene shell (in a similar way as nutrients delivering within skeleton networks of plant leaves), that is, ion-accessible surface areas of active materials are optimized[27,28]. Benefiting from the unique leaf-skeleton architecture and outstanding properties of carbon nanomaterials, the LSMCS electrodes reveal an electrical sheet resistance of ~1.8 Ω/sq at optical transmittance in the range of 85–88% and an areal capacitance of 7.06 mF cm^{-2} (measured at 0.78 mA cm^{-2} in a three-electrode cell) in 1 M Na_2SO_4 aqueous electrolyte. Based on the LSMCS electrodes, flexible transparent and symmetric SCs with PVA/H_3PO_4 gel electrolyte could operate stably at a large voltage of 1.6 V and outperform most reported SCs at comparable transmittances in terms of power and energy density, mechanical flexibility, and cycle stability.

Results

Flexible transparent and conductive LSMCS networks. Catalytic pyrolysis of sacrificial leaf-skeletons in combination with surface precipitation of carbon on metals are employed to fabricate LSMCS electrodes. We find out that leaf age is a significantly important factor to determine the formation of 3D spongy carbon core and thereby the flexibility of LSMCS electrodes. Leaves with age younger than 3 months, since their initial growth from shoot apical meristem are applicable for the transformation of their corresponding leaf-skeletons into 3D spongy carbon counterparts, which are enveloped by the robust graphene-based shell, accordingly bestowing mechanical flexibility for resultant LSMCS electrodes. In a striking contrast, pyrolysis of leaf-skeletons derived from older leaves result in non-spongy and brittle electrodes; these inflexible and fragile features are in good agreement with all previous reports on carbonization/activation of plant components for energy storage applications[29,30]. Detailed morphology observation and discussion on the leaf age effects can be found in Supplementary Figs. 1–6 and Supplementary Notes 1 and 2. Based on a study on effects of CVD parameters such as temperature and deposition time, the LSMCS electrodes processed at 800 °C with carbon deposition time of 6 min reveal the most expected features in terms of desired morphology, structural integrity, and flexibility (Fig. 1, Supplementary Figs. 7 and 8 and Supplementary Note 3), and therefore are selected for investigation thereafter.

Figure 1a shows a typical photograph of the as-fabricated LSMCS electrode, which resembles morphology and structure of its original leaf-skeleton network, demonstrating its transparent characteristic (optical transmittance of 85–88%, measured by UV–Vis spectroscopy). The LSMCS electrode is an accurate replication of the leaf-skeleton network (consisting of interconnected veins), which is derived from plant leaves gathered in nature, accordingly retaining the high transparency. This electrode is in a striking contrast to the reported leaf-vein inspired graphene film electrode[31], where the active material (reduced graphene oxide) serves as a micrometer-thick blade/mesophyll film embedded with nanochannels/nanoveins, i.e., non-transparent electrode.

Top view scanning electron microscopy (SEM) image (Fig. 1b) indicates that the LSMCS electrode is a hierarchical reticulated monolith of leaf-skeleton mimicked conduits surrounded by macroscopic spaces, thus allowing optical light to pass through. Higher magnification SEM images (Fig. 1c–e) reveal that lateral surface of the leaf-skeleton mimicked conduit is hierarchically rough and decorated with microscopic holes, therefore providing

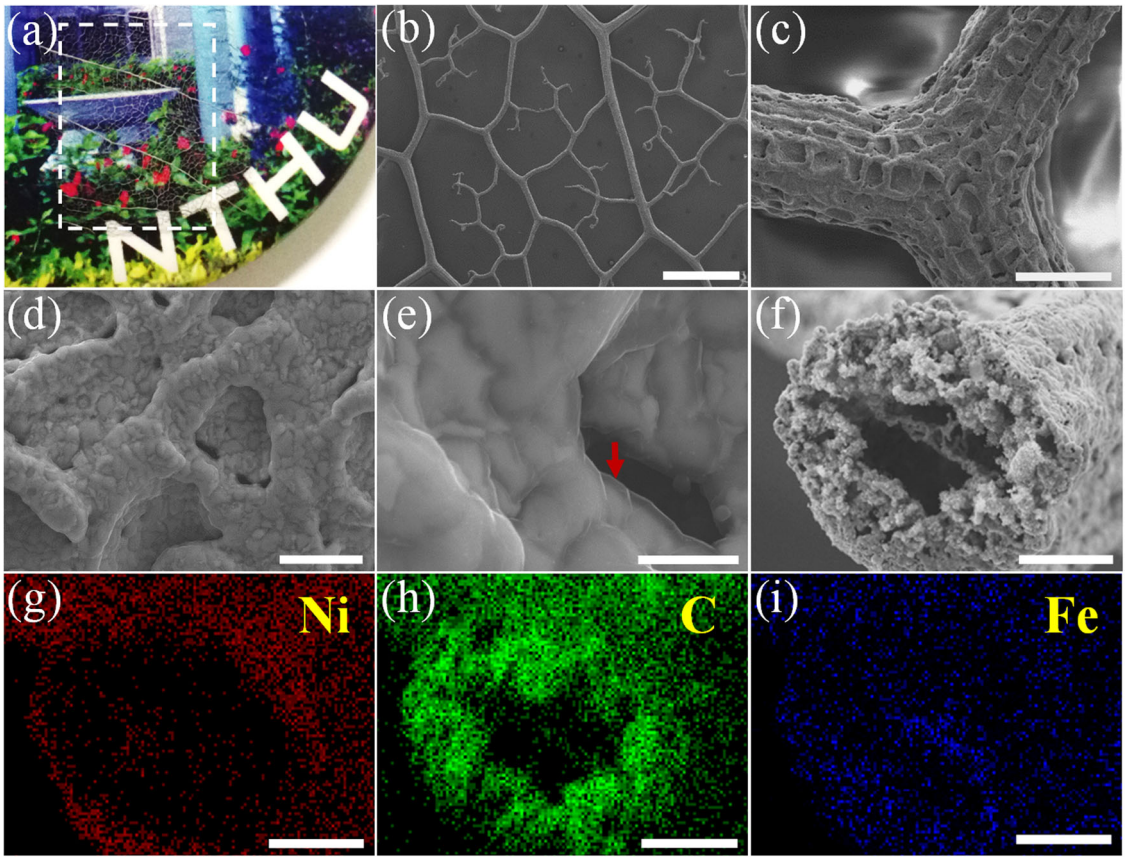

Fig. 1 Characterization of a freestanding flexible transparent LSMCS electrode. **a** A photograph of the electrode displaying its highly optical transparency. **b**–**e** Top view SEM images of the electrode at different magnifications. **f** A cross-sectional view SEM image of a conduit of the electrode revealing a core–shell structure. **g**–**i** EDX mapping of Ni, C, and Fe elements, respectively, acquired on the conduit shown in **f**. Scale bar in **b** is 500 μm, in **c** 30 μm, in **d** 5 μm, in **e** 1 μm, and in **f**–**i** 10 μm.

numerous pathways for electrolyte ions accessing into the conduit core from outside. The presence of graphene film on lateral surface of the conduit can be verified by a thin layer (Fig. 1d, e) with sharp edges (indicated by a red arrow in Fig. 1e) and wrinkles/ripples induced by difference in thermal coefficients between graphene and nickel[32]. Cross-sectional view SEM images (Fig. 1f, Supplementary Fig. 9a–d) of a leaf-skeleton-mimicked conduit obviously reveals a hollow core–shell structure, where interconnected nanocarbons exhibit as a 3D spongy core, graphene–nickel as a protective shell, and hollow space as a channel for electrolyte ion transport and storage. There exist numerous interfacial junctions between nanocarbons and interior surface of graphene–nickel shell and among nanocarbons themselves (Supplementary Fig. 9c, d), accordingly offering innumerable conductive paths for electrolyte ions transporting throughout the electrode, from cores to shells and cores to cores over all leaf-skeleton-mimicked conduits. Elemental analysis by energy-dispersive X-ray (EDX) mapping reveals that the core–shell conduit mainly composed of carbon (80.23 at.%), nickel (7.77 at.%), and iron (8.96 at.%), as shown in Fig. 1g–i and Supplementary Fig. 10. A minor quantity of oxygen (3.04 at.%) is probably attributed to incomplete reduction of iron oxides induced during pyrolysis of the $FeCl_3$ infiltrated leaf-skeleton, as well as the incomplete decomposition of the plant component. Additionally, auger electron spectroscopy analysis determines that carbon is main element on surfaces of spongy carbon core and graphene–nickel shell (Supplementary Fig. 11). Graphitic nature of the shell and core is evidenced by Raman characteristic peaks (D, G, and 2D) and their corresponding intensity ratios (Supplementary Fig. 12). The shell is evaluated to possess highly graphitic quality (large I_G/I_D ratio, beneficial for high conductivity), while the core contains more defects (small I_G/I_D ratio, favorable for charge storage); moreover, higher I_{2D}/I_G ratio suggests ultrathin nature of the graphene shell formed through a surface precipitation of carbon on nickel[33]. The ultrathin characteristic of the graphene shell is also confirmed by its high electron transparency (Supplementary Fig. 13).

Microstructure of the LSMCS electrode was further inspected by transmission electron microscopy (TEM). The graphene shell exhibits thin layered features with wrinkles and corrugations (Fig. 2a, b). Additionally, electron diffraction pattern (the inset of Fig. 2a) confirms a typical hexagonal crystalline structure of the graphene shell. The 3D spongy carbon core is observed as interconnected whisker-like and bead-like nanoparticles with sizes of several tens to hundreds nanometers (Fig. 2c and Supplementary Fig. 9). Especially, the junctions between the nanoparticles can be perceived as crumple graphitic nanosheets (Fig. 2c, d). These springy nanosheets are thus believed not only to provide mechanical flexibility and electrical pathways, but also offer plentiful active sites for charge storage[34]. Zoom-in TEM images (Fig. 2e, f) of a typical carbon nanoparticle indicate that it is composed of iron carbide encapsulated in a thick graphitic layer (Fig. 2e, f), in good agreement with XRD result (Supplementary Fig. 14).

It is noting that graphitic carbon-encapsulated iron carbide particles have been proved to hold outstanding chemical stability in severely acidic and basic environments[35], thus the spongy carbon core is anticipated to be highly stable in various

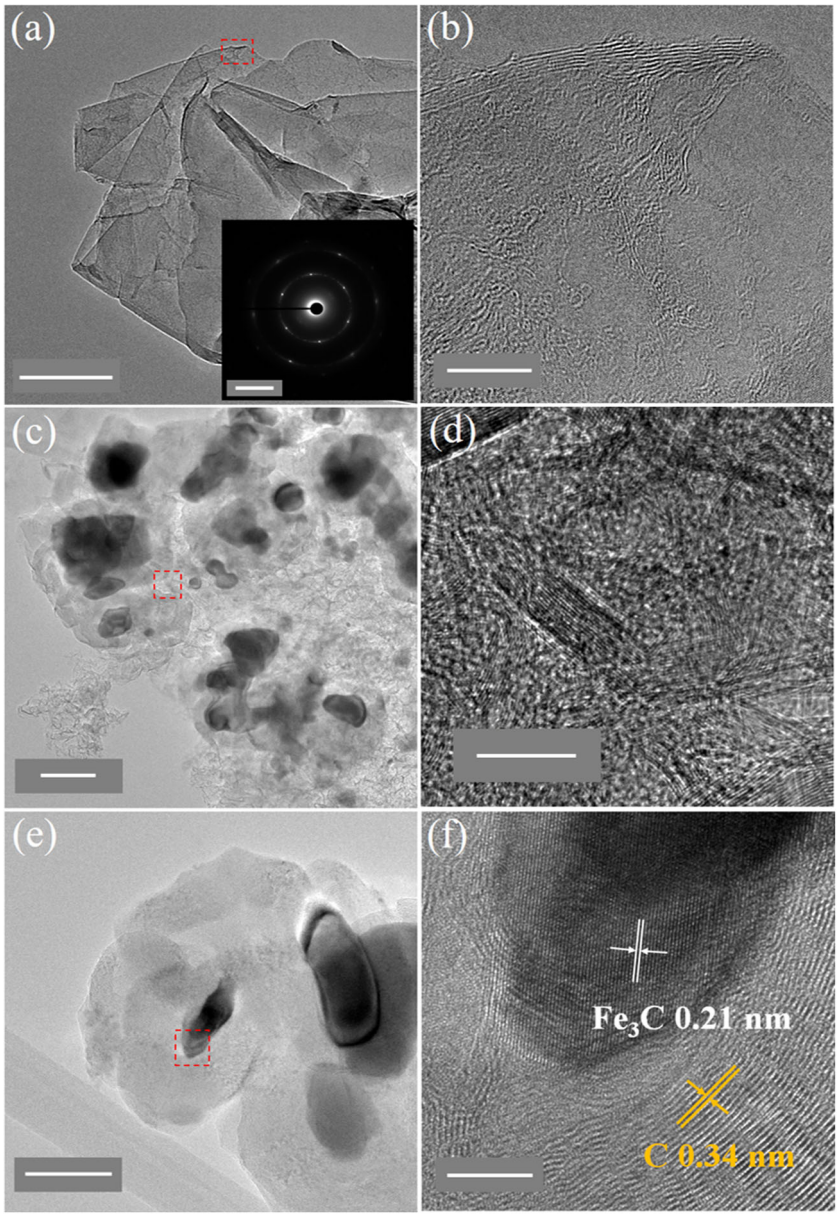

Fig. 2 TEM characterization of shell and core components of the LSMCS electrode. **a**, **b** TEM images of the graphene shell extracted from the electrode revealing graphitic layered structure; inset in **a** is an electron diffraction confirming the crystallinity of the graphene shell. **c**, **d** TEM images of the spongy carbon core comprising interconnected carbon nanoparticles and crumpled graphitic nanosheets. **e**, **f** High magnification TEM images of carbon nanoparticles, which are composed of iron carbide encapsulated in thick graphitic layers. Red-dotted rectangles in **a**, **c**, and **e** are marked areas corresponding to their high magnification images shown in **b**, **d**, and **f**, respectively. White scale bar in **a** is 100 nm, in the inset of **a** 5 1/nm, in **b** 10 nm, in **c** 100 nm, in **d** 10 nm, in **e** 50 nm, and in **f** 5 nm.

electrolytes. Owing to the monolithic structure made from the spongy carbon core and robust graphene-based shell, the freestanding LSMCS electrodes could perform remarkable flexibility and conductivity (Supplementary Fig. 15 and Supplementary Note 4), showing promise for practical uses as flexible transparent conductors and binder-free electrodes for flexible transparent SCs.

Electrochemical characterization of the LSMCS electrode. Electrochemical performance of the LSMCS electrode was studied in a standard three-electrode cell in 1 M Na_2SO_4 aqueous electrolyte. Figure 3a shows typical cyclic voltammetry (CV) curves of the LSMCS electrode under a scan rate of 500 mV s^{-1} at different potential windows from 1.0 V (−0.5 to 0.5 V) to 2.0 V (−1.0 to 1.0 V). All CV curves present nearly rectangular shapes, even at a large potential window of 2.0 V, displaying a great promise for development of high-energy density SCs. It is noteworthy that widening potential window (V) of SC electrodes is more efficient to achieve higher energy density (E) rather than increasing their specific capacitance (C) according to the equation $E = 1/2CV^2$[25]. In general, potential window (or working voltage) of aqueous SCs is strongly dependent on pH values of electrolytes, with which alkaline and acidic ones deliver lower working voltage (around 1.0 V) compared to neutral ones (up to 1.6–2.2 V)[36–38]. The wider potential windows in neutral electrolytes can be ascribed to low concentrations of H^+ and OH^- ions, which hinder oxygen/hydrogen evolution reactions[38].

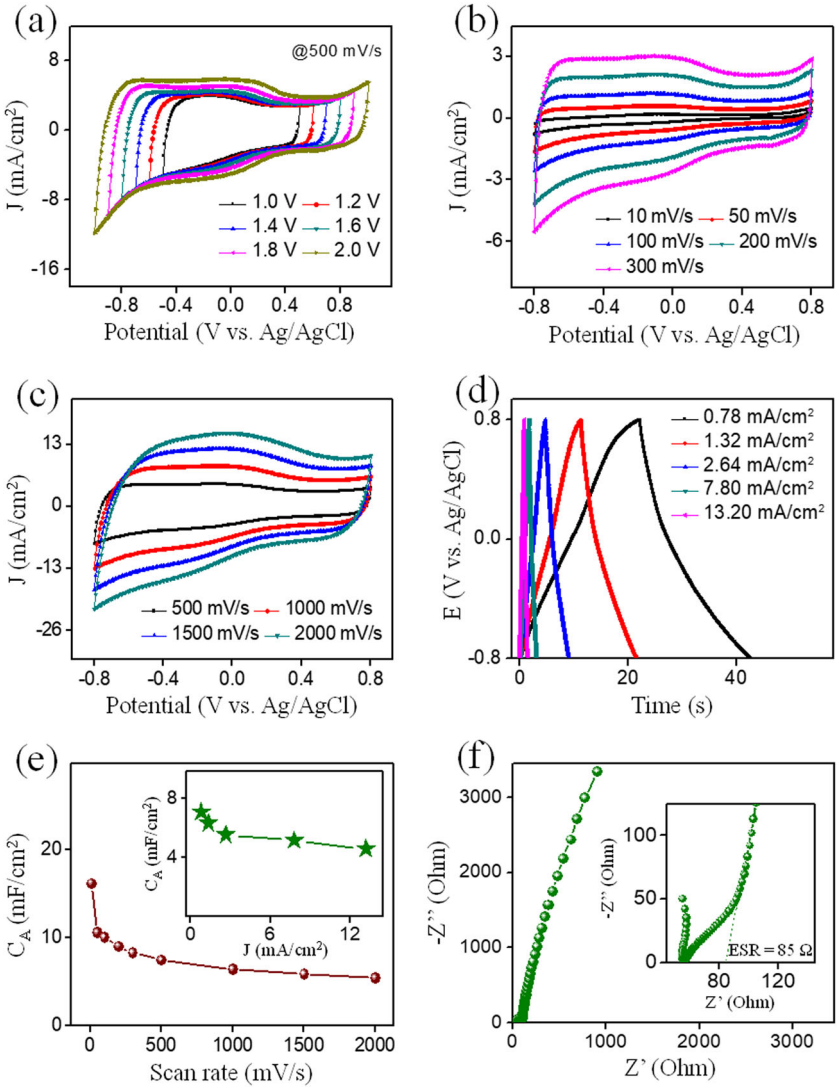

Fig. 3 Electrochemical properties of the LSMCS electrode. **a** Cyclic voltammetry (CV) of the electrode at different potential windows. **b**, **c** CV curves of the electrode at a potential window of 1.6 V under various scan rates from 10 to 2000 mV s^{-1}. **d** Galvanostatic charge–discharge curves of the electrode at various current densities. **e** Areal capacitance versus scan rate; inset shows areal capacitance versus current density. **f** Nyquist plot for the electrode; inset shows a zoom-in of the high-frequency part.

Nevertheless, structure of electrode materials is also considered the key issue to determine the width of potential window. For example, wall/sheet edges and defects of carbon nanomaterials could provide abundant active sites for hydrogen adsorption, where nascent hydrogen is strongly adsorbed, intercalated, and then trapped into spaces around active sites[39,40]. In this regard, we performed the electrochemical measurement in an acidic aqueous electrolyte using the LSMCS electrode (after Ni removal) to probe how large the potential window could be obtained. Interestingly, the LSMCS electrodes could operate firmly at a potential window of 1.6 V in 1 M H_3PO_4 aqueous electrolyte without capacitance fade after 10,000 cycles (Supplementary Fig. 16), suggesting a negligible dependence on pH value.

Through evaluation of electrochemical performance of the LSMCS electrodes in terms of areal capacitance, energy and power density, and cycle stability (Supplementary Fig. 17), a potential window of 1.6 V (from −0.8 to 0.8 V versus Ag/AgCl) was selected for subsequent characterizations. The quasi-rectangular shapes of CV curves (Fig. 3b and c) acquired at various scan rates, from 10 to 2000 mV s^{-1}, are indicative of practically ideal capacitive performance with ultrafast rates. This behavior is further confirmed by the galvanostatic charge/discharge (GCD) curves (Fig. 3d), which display nearly symmetric and triangular shapes without obvious IR drops at different current densities. Figure 3e and its inset show areal capacitances (C_A) of the LSMCS electrode as functions of scan rate and applied current density, extracted from CV curves (Fig. 3b, c) and GCD curves (Fig. 3d), respectively. At a low scan rate of 10 mV s^{-1}, C_A is calculated to be 16.17 mF cm^{-2}, which is decreased to 5.41 mF cm^{-2} as the scan rate is increased to 2000 mV s^{-1}; comparable C_A values (7.06–4.58 mF cm^{-2}) can be also obtained under applied current density in the range of 0.78–13.2 mA cm^{-2}. These C_A performances (at $T = 85$–88%) are superior than those (also measured in three-electrode configuration) of other transparent SC electrodes, including $Ti_3C_2T_x$ nanosheets (3.4 mF cm^{-2} at $T = 40\%$)[2], RuO_2/PEDOT:PSS (2.2 mF cm^{-2} at $T = 89\%$)[13], PEDOT:PSS (1.9 mF cm^{-2} at $T = 70\%$)[14] or carbon nanotubes (0.1 mF cm^{-2} at $T = 90\%$)[41]. It is worth noting that the working potential windows of our LSMCS electrodes are larger (1.6–2.0 versus 0.6–0.8 V), thus possessing much higher energy densities. The greater performance of our LSMCS electrode can be attributed to the unique design of LSMCS conduit structures. The 3D spongy

carbon core consists of moderately defective carbon nanoparticles, which are interconnected via crumple graphitic nanosheets, thus providing numerous active sites and conductive paths for electrolyte ion adsorption and transport. Significantly, the hollow interconnected channels (Fig. 1f) within the conduits could serve as interconnected reservoirs for storing electrolyte entirely inside the electrode, thus providing close and direct diffusion pathways for electrolyte ions accessing to spongy carbon cores from conduit centers and facilitating ions to transport throughout the electrode cores. Moreover, microscopic holes on the shell surfaces (Fig. 1c–e) also serve as directly open channels for ion diffusion into the carbon core and interior surface of graphene shell from outside of the electrode. In other words, the porosity and abundance of active sites of the 3D spongy carbon core in combination with the dual ion diffusion pathways (from outward and inward of the core) are believed to provide large ion-accessible surface area and plentiful diffusion routes with short lengths and low tortuosity, thus facilitating the access of electrolyte ions to entire active materials (spongy carbon core and graphene shell), i.e., high capacitive performance.

Figure 3f shows a Nyquist plot obtained for the LSMCS electrode in a frequency range of 0.1–100 kHz with a 5.0 mV AC amplitude; a zoom-in view at the high-frequency region is included in the inset. The line almost vertical to the axis of the real component of impedance in the low-frequency region indicates an ideal capacitive behavior of the LSMCS electrode. The magnitude of equivalent series resistance was estimated to be ~85 Ω by extrapolating the vertical portion of the plot to axis of the real part (inset in Fig. 3f). Furthermore, there was no capacitance degradation found as the LSMCS electrode subjected to 10,000 cycles at the potential window of 1.6 V (Supplementary Fig. 17c), indicating its highly electrochemical stability. This can be accredited to the robust graphene-based shell, which protects and prevents fragmentation of the active carbon core during charge/discharge cycles, thus leading to the good capacitance retention. As a proof of concept, electrochemical performance of aqueous SCs using a pair of the LSMCS electrodes assembled as in-plane configuration was examined, showing promise for development of high voltage SCs (Supplementary Fig. 18 and Supplementary Note 5).

Electrochemical performance of solid state SC devices. In order to exploit the high capacitive performance of our LSMCS electrodes for possible uses in energy storage devices for flexible transparent electronics, solid state SC devices assembled as in-plane configuration with PVA/H_3PO_4 gel electrolyte were fabricated and characterized. Figure 4a and its inset, respectively, show photographs of an all solid state SC device at bending and flat states, representing its flexibility and transparency with optical transmittance of ~80% (Supplementary Fig. 19a). Figure 4b shows the voltage-dependent CV characterization of the SC device at a scan rate of 500 mV s^{-1}, revealing the maintenance of quasi-rectangular shapes of CV curves as working voltage is increased from 1.0 to 2.0 V.

Similarly, GCD was also carried out at 66.9 μA cm^{-2} with different working voltages ranging from 1.0 to 2.0 V (Supplementary Fig. 19b); all charge parts of the GCD curves overlap while their discharge parts are nearly parallel, inferring an excellent SC performance. At the selected voltage of 1.6 V, CV curves of the SC device exhibit well-rectangular shapes even at scan rates higher than 800 mV s^{-1} (Fig. 4c and Supplementary Fig. 19c), suggesting a high rate capability. A pair of redox waves observed in the CV curves possibly involves Faradaic reactions of oxygen-containing functional groups[42,43], which were generated on surfaces of the graphene shell and spongy carbon core during Ni removal process using the phosphoric acid etchant. Possible Faradaic reactions ascribed to the redox waves can be considered as follows:[44]

$$-\mathrm{COOH} \Leftrightarrow -\mathrm{COO} + \mathrm{H}^+ + \mathrm{e}^-, \quad (1)$$

$$>\mathrm{C}-\mathrm{OH} \Leftrightarrow >\mathrm{C}=\mathrm{O} + \mathrm{H}^+ + \mathrm{e}^-, \quad (2)$$

$$>\mathrm{C}=\mathrm{O} + \mathrm{e}^- \Leftrightarrow >\mathrm{C}-\mathrm{O}^- \quad (3)$$

The GCD curves (Fig. 4d) of the device collected at various current densities from 22.3 to 178.4 μA cm^{-2} are in consistence with CV curves as verified by the slight distortion from triangle shapes. Figure 4e and its inset show C_A of the SC device as functions of scan rate and current density, extracted from CV and GCD curves shown in Fig. 4c, d, respectively. The resultant C_A values estimated to be in the ranges of 0.11–0.19 mF cm^{-2} (at scan rates of 5000–10 mV s^{-1}) and 0.18–0.23 mF cm^{-2} (current densities of 178.4–22.3 μA cm^{-2}), outperforming most previously reported transparent solid SCs based on carbon nanomaterials including carbon nanotubes (0.15 mF cm^{-2})[20], CVD graphene (4.27×10^{-3}–5.8×10^{-3} mF cm^{-2})[21,22] or graphene–graphene quantum dot hybrid (0.01 mF cm^{-2})[23]. Although higher C_A values (0.23–0.87 mF cm^{-2}) were reported for SC devices based on thin films of RuO_2/PEDOT[13], PEDOT:PSS[14], and $Ti_3C_2T_x$[2], their narrower working voltages (0.6–0.8 V) are impediments that cause lower energy densities (E_A) according to equation $E_A = 1/2C_AV^2$.

To demonstrate device scalability for meeting different demands on higher capacitance and voltage, two SCs were connected in series and parallel; their CV and GCD characteristics were recorded, as shown in Fig. 4f, g, respectively. The parallel assembly reveals a capacitance (or a CV area) almost as twice as that of individual SCs while the series one could extend the working voltage to 3.2 V, which is two times larger as compared to that of individual SCs (Fig. 4f). In addition, the two SCs connected in series display a 3.2 V window at similar charge/discharge time as compared with the individual SCs operating at 1.6 V; the discharge time of the two SCs connected in parallel is approximately two times of that of individual SCs when operated at the same current density (Fig. 4g). These device assemblies indicate that resultant capacitance/voltage is well-matched with circuit laws, suggesting a good scalability for constructing power supplies to meet different applications. To assess device flexibility, CV measurement on the SC device under various bending conditions and cycles were executed. As shown in Fig. 4h, CV curves of the device under flat condition, flexed configuration with a bending angle θ (as graphically defined in inset of Fig. 4h) ranging from 60° to 150°, and release state mostly remain unchanged, signifying the outstanding flexibility of the device. Such capacitive performance under flexed conditions was further confirmed by a combined cycling test where no capacitance degradation was found after 30,000 flat-bend-release cycles (Fig. 4i and its inset).

The overall electrochemical performance of our devices is evaluated by Ragone plots, presenting a comparison to other flexible transparent devices (Fig. 5). On average, energy and power density of our SC devices were calculated to be ~0.335 μWh cm^{-2} and 313.25 μW cm^{-2} (aqueous device) and ~0.068 μWh cm^{-2} and 47.08 μW cm^{-2} (solid device), respectively. These SCs outperform flexible transparent devices based on $T_3C_2T_x$ nanosheets[2], RuO_2/PEDOT[13], PEDOT:PSS[14], graphene/graphene quantum dots[23], CVD graphene and reduced graphene oxide[45], and graphene/silver nanowires[46]. A more detailed comparison on the values of energy and power density of various SC devices are given in Supplementary Table 1.

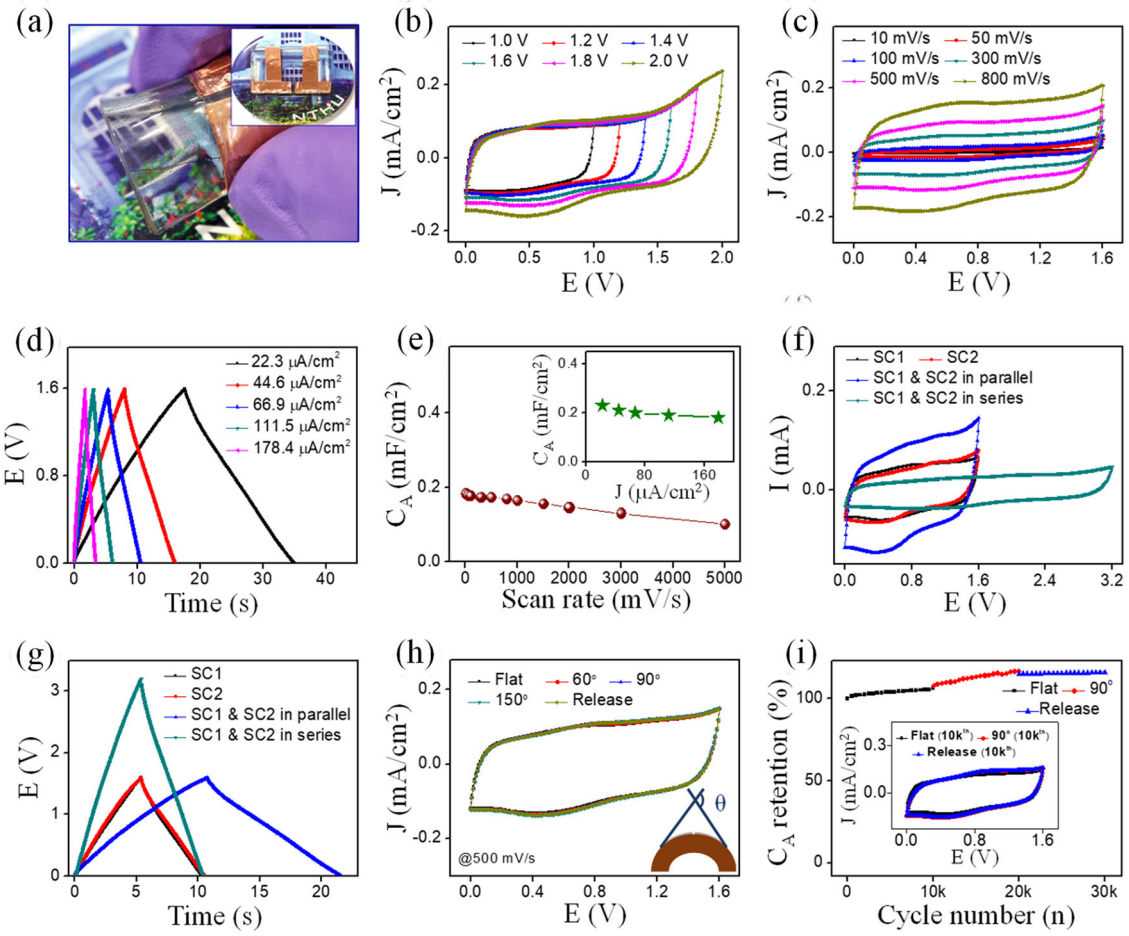

Fig. 4 Flexible transparent solid-state SCs based on the LSMCS electrodes. **a** A typical photograph of the flexible transparent SC device under a bending state; inset shows the SC at a flat state. **b** CV curves at a scan rate of 500 mV s^{-1} under various working voltages. **c**, **d** CV and GCD curves under a working voltage of 1.6 V at different scan rates and current densities, respectively. **e** Areal capacitance versus scan rate; inset shows areal capacitance versus current density. **f** CV curves at a scan rate of 500 mV s^{-1} and **g** GCD curves under a current density of 66.0 μA cm^{-2}, respectively, of the two SC devices in individual, parallel, and series. **h** CV curves of the device under various bending angles; the inset graphically defines a bending angle θ. **i** Cycling stability of the SC under flat, bend, and release states; inset shows selected CV curves at different states.

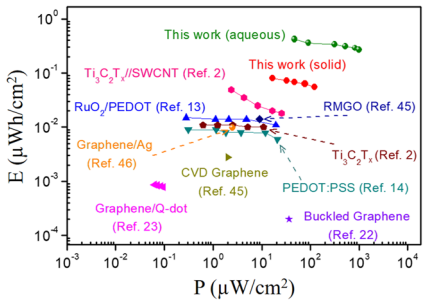

Fig. 5 Energy and power density of various transparent SC devices. Ragone plots of aqueous and solid SC devices based on the LSMCS electrodes and a comparison to other transparent devices.

Discussion

It is acknowledged that plant components consist of hierarchically ordered structures of interconnected channels that allow efficient transport of nutrients throughout the entire plants. These plant structures have been an inspiration for a considerable number of studies in designing artificial materials for various applications, especially in energy storage[6,47–49]. For the use as electrode materials in energy storage devices, thermal activation/carbonization of plant components is an indispensable step[6,47–49]. Nevertheless, thermally activated/carbonized plant components are brittle and fragile due to the disruption of most inter and intramolecular hydrogen, C–C, and C–O bonds; that is the channel structure is completely destroyed as the plant components lose their fibrous nature[49]. Accordingly, the activated/carbonized product must be ground into tiny powder, followed by a combination with binders to prepare electrodes for energy storage devices. Binder-free, monolithic shape of activated wood has been recently reported as efficient SC electrodes owing to the unique channel structures within the wood[6]. However, the activated wood electrode has been presented as a thick block, thus their potential use in fully flexible transparent electronic devices is limited. In a striking contrast, we find out that by selecting proper conditions, a plant component can be not only shape maintained but also function endowed with flexibility after a thermal carbonization/activation process. Specifically, the transformation of young leaf-skeleton networks into spongy carbon counterparts can be achieved by the thermal decomposition of skeletons using $FeCl_3$ catalyst. On heating at high temperature (800 °C), biopolymers of the skeletons and $FeCl_3$ are simultaneously decomposed into iron compound (iron oxides/carbides) particles (Supplementary Fig. 6 and Supplementary Note 2), consequently catalyzing the formation of nanocarbons during the introduction of

methane and hydrogen gases. On the other hand, old leaf-skeleton networks could not be transformed into spongy carbon counterparts. It is noticed that the processed old leaf-skeletons remain unchanged in morphology (Supplementary Fig. 4 and Supplementary Note 1), but become brittle and fragile as generally recognized in carbonized/activated plant components. This discrepancy can be ascribed to difference in crystallinity degree and size of biopolymers presented in the two types of skeleton networks. The older is more resilient and possesses greater crystalline degree[50], therefore being more resistant and inert to the catalytic pyrolysis.

The unique core–shell structures of the LSMCS electrodes, where the 3D spongy carbon is wrapped and protected by the robust graphene-based film, are believed to play a vital role for achieving large potential windows. In particular, microscopic spaces within crumple graphitic nanosheets, defects on graphitic layers (Fig. 2c–f), and interstitial voids among carbon nanoparticles (Fig. 2c, Supplementary Fig. 9) of the spongy core could function as efficient "traps" for nascent hydrogen/oxygen intercalation and storage[39,40]. Such hydrogen/oxygen confinement within the spongy core could be further preserved by the robust graphene-based shell, leading to enhanced inhibition of gas liberation to the electrolytes from the electrode core. In addition, the superior performance of the solid SC devices can be ascribed to the monolith of hierarchically interconnected conduits of the LSMCS electrodes. This novel design provides a number of advantages as follows: (i) the 3D spongy carbon core with abundance of active sites, such as defects and microscopic interstices among the carbon nanoparticles and crumple graphitic nanosheets, which offer large ion-assessable surface area and high working voltage (i.e., large capacitance and high energy density), (ii) the dual ion diffusion pathways with low tortuosity given by microscopic holes on exterior surface of the graphene-based shells and interconnected hollow channels within the conduits, which facilitate the access of electrolyte ions to the carbon core (i.e., fast rates), and (iii) the strongly robust and highly conductive graphene-based shells, which preserve the structural integrity and enhance electrical conductivity of the 3D spongy carbon cores (i.e., excellent capacitance retention under flexed conditions).

In summary, using selected leaf-skeleton networks as sacrificial templates, we have developed a method to fabricate freestanding, flexible transparent, and conductive electrodes, consisting of core–shell-structured conduits, in a CVD process. Owing to the unique structural and material design, the electrodes exhibit a low electrical sheet resistance of ~1.8 Ω/sq at optical transmittance of 85–88% and a high areal capacitance of 7.06 mF cm^{-2} in 1 M Na_2SO_4 aqueous electrolyte. Flexible transparent and symmetric SCs, made entirely from the electrodes without binders/additives, could operate stably at a large voltage of 1.6 V in PVA/H_3PO_4 gel electrolyte without capacitance degradation after 30,000 flat-bend-release cycles. The solid devices deliver an averaged energy and power density of 0.068 μWh cm^{-2} and 47.08 μW cm^{-2}, respectively, displaying highest values among SCs at comparable optical transmittances. We believe our fabrication methodology provides a promising strategy towards development of multi-functional, freestanding, and conductive core–shell architectures based on composites of graphene and other exciting nanomaterials, which can be designed by employing various biological/artificial templates and precursors.

Methods

Fabrication of LSMCS electrodes. Bodhi (or *Magnolia alba*) leaves with average sizes of ~8 × 13 cm^2 were collected during June–August and washed with clean water. The leaves were immersed in an aqueous solution of 0.1 mg mL^{-1} KOH at 80 °C for 2 h. Mesophyll of the as-boiled leaves was then removed by sonicating the boiled leaves in water for few minutes, consequently leaving leaf-skeleton networks. The leaf-skeleton networks were finally immersed in clean water overnight.

As-prepared leaf-skeleton networks were immersed in a 30 mg mL^{-1} $FeCl_3{\cdot}6H_2O$ solution in ethanol for a day, followed by drying at 50 °C overnight. The dried, $FeCl_3$ infiltrated leaf-skeleton networks were then coated with 500 nm-thick Ni on both sides by a sputtering method, resulting Ni coated and $FeCl_3$ infiltrated leaf-skeleton networks.

In a typical CVD process, the Ni coated and $FeCl_3$ infiltrated network was heated to 800 °C at a heating rate of 10 °C/min and hold at the temperature for 1 h in Ar (500 sccm) at a pressure of ~600 Torr. Subsequently, CH_4 (60 sccm) and H_2 (100 sccm) gases were simultaneously introduced into the reactor for 6 min. Finally, the sample was cooled down to room temperature within 20 min.

Material characterizations. The morphological transformation from leaf-skeleton networks to LSMCS electrodes were observed using a field emission electron microscope (FESEM, JEOL JSM-6500F) and elemental compositions of the LSMCS electrodes were analyzed by an accompanied EDX spectroscope and an Auger spectroscope. Crystalline and graphitic structures of the graphene-based shell and carbon core were examined by a transmission electron microscope (JEOL JEM3000F FE-TEM), a Raman spectroscope (Horiba Jobin Yvon LabRam HR800) with a 632.8 nm He–Ne laser, and an X-ray diffractometer (D2 Phaser, Bruker). Optical transmittance of the LSMCS electrodes and their assembled devices were measured using a UV-Vis spectrophotometer (V-670, Jasco).

Fabrication of aqueous and solid state SCs. An in-plane configuration consisted of two identical LSMCS electrodes were utilized for fabrication of both aqueous and solid devices. Typically, a pair of the LSMCS electrodes were located on a polydimethylsiloxane substrate and kept in parallel at a distance of ~2.0 mm; copper tapes were partially contacted with each electrode for the characterization of electrochemical performance. A thin layer of a Scotch glue was partly pasted between copper tapes and electrodes to prevent diffusion of electrolytes into copper. For aqueous devices, the electrolyte is 1 M Na_2SO_4 solution and Ni is remained in the electrodes. On the other hand, PVA/H_3PO_4 electrolyte gel is used for solid devices. Before gel coating, the LSMCS electrodes were immersed in 1 M H_3PO_4 for 2 days to remove Ni, followed by drying in a fume hood at ambient conditions. Gel electrolyte solution was prepared by mixing 3.0 g of PVA with 3.0 g of H_3PO_4, followed by vigorous stirring at 85 °C until the solution became clear. The gel electrolyte solution was finally coated over the two electrodes and dried in a fume hood at room temperature to allow the gel electrolyte to solidify.

Electrochemical measurement. The electrochemical performance of the LSMCS electrode was investigated by CV, GCD, and EIS measurements using a potentiostat/galvanostat (Autolab PGSTAT30 and FRA2). A three-electrode configuration in 1 M Na_2SO_4 electrolyte was employed, with which a Pt plate served as a counter electrode, Ag/AgCl as a reference electrode, LSMCS electrode as a working electrode. Before measurement, the LSMCS electrode was mildly treated by air plasma (50 W, 30 s), followed by immersion in the electrolyte for a day. Areal capacitance of the LSMCS electrodes and their devices was calculated from CV curve according to Eq. (1): $C_A = \frac{1}{2Av\Delta V}\int_i^f I(V)\mathrm{d}V$ (1), where A (cm^2) is area of electrodes buried/immersed in electrolytes, v (V s^{-1}) the scan rate, and ΔV (V) the voltage/potential window. Areal capacitance was also calculated from GCD curve using Eq. (2): $C_A = \frac{2I}{V^2}\int V\,dt$ (2), where I (A) is the applied charge–discharge current, A (cm^2) the electrode areas in contact with electrolytes, V is voltage after the IR drop, $\int V\,dt$ is integral area under discharge curve after IR drop. Energy density and power density of the devices were calculated using Eq. (3) and (4): $E = \frac{1}{2}\frac{1}{3600}C_A\Delta V^2$ (3), $P = 3600E/\Delta t$ (4), where E is energy density (μWh cm^{-2}), C_A (mF cm^{-2}) the areal capacitance calculated from GCD curves, ΔV (V) the operating voltage window, P the power density (μW cm^{-2}), and Δt (s) the discharge time.

Data availability

The main data that support the findings of this study are available within the article and its Supplementary Information file. Other relevant data are available from the corresponding author upon reasonable request.

Received: 17 April 2019; Accepted: 14 October 2019;
Published online: 29 November 2019

References

1. Liang, B. Y. et al. Flexible transparent molybdenum trioxide nanopaper for energy storage. *Adv. Mater.* **28**, 6353–6358 (2016).
2. Zhang, C. et al. Transparent, flexible, and conductive 2D titanium carbide (MXene) films with high volumetric capacitance. *Adv. Mater.* **29**, 1702678 (2017).

3. Liu, Y. H. et al. Freestanding transparent metallic network based ultrathin, foldable and designable supercapacitors. *Energy Environ. Sci.* **10**, 2534–2543 (2017).
4. Ginting, R. T., Ovhala, M. M. & Kang, J. W. A novel design of hybrid transparent electrodes for high performance and ultra-flexible bifunctional electrochromic-supercapacitors. *Nano Energy* **53**, 650–657 (2018).
5. Simon, P. & Gogotsi, Y. Materials for electrochemical capacitors. *Nat. Mater.* **7**, 845–854 (2008).
6. Chen, C. et al. All-wood, low tortuosity, aqueous, biodegradable supercapacitors with ultra-high capacitance. *Energy Environ. Sci.* **10**, 538–545 (2017).
7. Choi, C. et al. Improvement of system capacitance via weavable superelastic biscrolled yarn supercapacitors. *Nat. Commun.* **7**, 13811 (2016).
8. Pan, Z. et al. High electroactive material loading on a carbon nanotube@3D graphene aerogel for high-performance flexible all-solid-state asymmetric supercapacitors. *Adv. Funct. Mater.* **27**, 1701122 (2017).
9. Wang, Z., Qin, Q., Xu, W., Yan, J. & Wu, Y. Long cyclic life in manganese oxide-based electrodes. *ACS Appl. Mater. Interfaces* **8**, 18078–18088 (2016).
10. Pang, S. C., Anderson, M. A. & Chapman, T. W. Novel electrode materials for thin film ultracapacitors: comparison of electrochemical properties of sol–gel-derived and electrodeposited manganese dioxide. *J. Electrochem. Soc.* **147**, 444–450 (2000).
11. El-Kady, M. F. et al. Engineering three-dimensional hybrid supercapacitors and microsupercapacitors for high-performance integrated energy storage. *Proc. Natl Acad. Sci. USA* **112**, 4233 (2015).
12. Lang, X., Hirata, A., Fujita, T. & Chen, M. Nanoporous metal/oxide hybrid electrodes for electrochemical supercapacitors. *Nat. Nanotechnol.* **6**, 232–236 (2011).
13. Zhang, C. et al. Highly flexible and transparent solid-state supercapacitors based on RuO2/PEDOT:PSS conductive ultrathin films. *Nano Energy* **28**, 495–505 (2016).
14. Higgins, T. M. & Coleman, J. N. Avoiding resistance limitations in high-performance transparent supercapacitor electrodes based on large-area high-conductivity PEDOT:PSS films. *ACS Appl. Mater. Interfaces* **7**, 16495–16506 (2015).
15. Yang, Z. et al. Carbon nanotube- and graphene-based nanomaterials and applications in high-voltage supercapacitor: a review. *Carbon* **141**, 467–480 (2019).
16. Ferrand, H. L. et al. Magnetic assembly of transparent and conducting graphene-based functional composites. *Nat. Commun.* **7**, 12078 (2016).
17. Estevez, L. et al. Hierarchically porous graphitic carbon with simultaneously high surface area and colossal pore volume engineered via ice templating. *ACS Nano* **11**, 11047–11055 (2017).
18. Xiong, G. et al. Bioinspired leaves-on-branchlet hybrid carbon nanostructure for supercapacitors. *Nat. Commun.* **9**, 790 (2018).
19. Lv, T., Liu, M., Zhu, D., Gan, L. & Chen, T. Nanocarbon-based materials for flexible all-solid-state supercapacitors. *Adv. Mater.* **30**, 1705489 (2018).
20. Niu, Z. et al. A repeated halving approach to fabricate ultrathin single-walled carbon nanotube films for transparent supercapacitors. *Small* **9**, 518–524 (2013).
21. Chen, T., Xue, Y., Roy, A. K. & Dai, L. Transparent and stretchable high-performance supercapacitors based on wrinkled graphene electrodes. *ACS Nano* **8**, 1039–1046 (2014).
22. Xu, P. et al. Laminated ultrathin chemical vapor deposition graphene films based stretchable and transparent high-rate supercapacitor. *ACS Nano* **8**, 9437–9445 (2014).
23. Lee, K. et al. Highly transparent and flexible supercapacitors using graphene-graphene quantum dots chelate. *Nano Energy* **26**, 746–754 (2016).
24. Benzigar, M. R. et al. Ordered mesoporous C70 with highly crystalline pore walls for energy applications. *Adv. Funct. Mater.* **28**, 1803701 (2018).
25. Song, Z. et al. High-energy flexible solid-state supercapacitors based on O, N, S-tridoped carbon electrodes and a 3.5 V gel-type electrolyte. *Chem. Eng. J.* **372**, 1216–1225 (2019).
26. Xue, D. et al. Template-free, self-doped approach to porous carbon spheres with high N/O contents for high-performance supercapacitors. *ACS Sustain. Chem. Eng.* **7**, 7024–7034 (2019).
27. Han, B. et al. Bio-inspired networks for optoelectronic applications. *Nat. Commun.* **5**, 5674 (2014).
28. Ronellenfitsch, H. & Katifori, E. Global optimization, local adaptation, and the role of growth in distribution networks. *Phys. Rev. Let.* **117**, 138301 (2016).
29. Chen, C. et al. Scalable and sustainable approach toward highly compressible, anisotropic, lamellar carbon sponge. *Chem* **4**, 544–554 (2018).
30. Biswal, M., Banerjee, A., Deo, M. & Ogale, S. From dead leaves to high energy density supercapacitors. *Energy Environ. Sci.* **6**, 1249–1259 (2013).
31. Chang, J. et al. Leaf vein-inspired nanochanneled graphene film for highly efficient micro-supercapacitors. *Adv. Energy Mater.* **5**, 1500003 (2015).
32. Nguyen, D. D. et al. Macroscopic, freestanding, and tubular graphene architectures fabricated via thermal annealing. *ACS Nano* **9**, 3206–3214 (2015).
33. Chae, S. J. et al. Synthesis of large-area graphene layers on poly-nickel substrate by chemical vapor deposition: wrinkle formation. *Adv. Mater.* **21**, 2328–2333 (2009).
34. Zang, J., Cao, C., Feng, Y., Liu, J. & Zhao, X. Stretchable and high-performance supercapacitors with crumpled graphene papers. *Sci. Rep.* **4**, 6492 (2014).
35. Hu, Y. et al. Hollow spheres of iron carbide nanoparticles encased in graphitic layers as oxygen reduction catalysts. *Angew. Chem. Int. Ed.* **53**, 3675–3679 (2014).
36. Fic, K., Lota, G., Meller, M. & Frackowiak, E. Novel insight into neutral medium as electrolyte for high-voltage supercapacitors. *Energy Environ. Sci.* **5**, 5842–5850 (2012).
37. Chae, J. H. & Chen, G. Z. 1.9 V Aqueous carbon-carbon supercapacitors with unequal electrode capacitances. *Electrochim. Acta* **86**, 248–254 (2012).
38. Bichat, M. P., Raymundo-Pinero, E. & Beguin, F. High voltage supercapacitor built with seaweed carbons in neutral aqueous electrolyte. *Carbon* **48**, 4351–4361 (2010).
39. Zhao, L. et al. Carbon nanofibers with radially grown graphene sheets derived from electrospinning for aqueous supercapacitors with high working voltage and energy density. *Nanoscale* **5**, 4902–4909 (2013).
40. Béguin, F., Presser, V., Balducci, A. & Frackowiak, E. Carbons and electrolytes for advanced supercapacitors. *Adv. Mater.* **26**, 2219–2251 (2014).
41. King, P. J., Higgins, T. M., De, S., Nicoloso, N. & Coleman, J. N. Percolation effects in supercapacitors with thin, transparent carbon nanotube electrodes. *ACS Nano* **6**, 1732–1741 (2012).
42. Pan, H., Poh, C. K., Feng, Y. P. & Lin, J. Supercapacitor electrodes from tubes-in-tube carbon nanostructures. *Chem. Mater.* **19**, 6120–6125 (2007).
43. Yu, D. et al. Scalable synthesis of hierarchically structured carbon nanotube-graphene fibres for capacitive energy storage. *Nat. Nanotechnol.* **9**, 555–562 (2014).
44. Frackowiak, E. & Beguin, F. Carbon materials for the electrochemical storage of energy in capacitors. *Carbon* **39**, 937–950 (2001).
45. Yoo, J. J. et al. Ultrathin planar graphene supercapacitor. *Nano Lett.* **11**, 1423–1427 (2011).
46. Zhong, Y. et al. Simultaneously armored and active graphene for transparent and flexible supercapacitors. *Adv. Funct. Mater.* **28**, 1801998 (2018).
47. Zhu, J. A hyperaccumulation pathway to three-dimensional hierarchical porous nanocomposites for highly robust high-power electrodes. *Nat. Commun.* **7**, 13432 (2016).
48. Yin, H. et al. Harvesting capacitive carbon by carbonization of waste biomass in molten salts. *Environ. Sci. Technol.* **48**, 8101–8108 (2014).
49. Tumuluru, J. S., Sokhansanj, S., Hess, J. R., Wright, C. T. & Boardman, R. D. A review on biomass torrefaction process and product properties for energy applications. *Ind. Biotechnol.* **7**, 384 (2011).
50. Jahan, M. S. & Mun, S. P. Effect of tree age on the cellulose structure of Nalita wood (*Trema orientalis*). *Wood Sci. Technol.* **39**, 367–373 (2005).

Acknowledgements

This research is financially supported by the Ministry of Science and Technology (Taiwan) through grant nos. 104-2221-E-007-029-MY3 and MOST 104-2811-E-007-06.

Author contributions

D.D.N. conceptualized the idea, designed the research, and performed experiments. N.-H.T. supervised the project. C.-H.H, P.-Y.H. and Y.-L.C. assisted the electrochemical and Auger electron spectroscopy measurements. D.D.N., T.-Y.S, and Y.-L.C. performed TEM measurement/analysis. The manuscript was written by D.D.N. with discussion from N.-H.T., C.-Y.L., and all other co-authors.

Competing interests

The authors declare no competing interests.

Additional information

Supplementary information is available for this paper at https://doi.org/10.1038/s42004-019-0238-9.

Correspondence and requests for materials should be addressed to N.-H.T.

Reprints and permission information is available at http://www.nature.com/reprints

Publisher's note Springer Nature remains neutral with regard to jurisdictional claims in published maps and institutional affiliations.